frontiers in Materials

ORIGINAL RESEARCH
published: 18 March 2021
doi: 10.3389/fmats.2021.648980

Synthesis and Characterization of a Hydroxyapatite-Sodium Alginate-Chitosan Scaffold for Bone Regeneration

*Dingkun Liu[1,2], Zhihui Liu[3], Jundong Zou[2], Lingfeng Li[2], Xin Sui[2], Bizhou Wang[2], Nan Yang[2] and Bowei Wang[1]**

[1] The Second Hospital, Jilin University, Changchun, China, [2] Jilin Provincial Key Laboratory of Tooth Development and Bone Remodeling, Hospital of Stomatology, Jilin University, Changchun, China, [3] Hospital of Stomatology, Jilin University, Changchun, China

Bone scaffolds play an important role in promoting the healing of large bone defects. However, the type of scaffold material, type of drug loaded into the scaffold, and method of preparation have a significant impact on the scaffold's properties. In this study, we developed a composite scaffold comprising sodium alginate (SA), chitosan (CS), and hydroxyapatite (HA). The composite stent carries vascular endothelial growth factor (VEGF), wrapped in internal microspheres, and vancomycin (VAN). The microspheres are wrapped in an outer matrix formed by SA, CS, and HA, whereas the outer matrix carries VAN. Using Fourier-transform infrared spectroscopy (FTIR), X-ray diffraction, and scanning electron microscopy analyses, we studied the contraction rate, swelling, porosity, mechanical properties, degradation, and drug release ability of all the composite scaffolds. The best scaffold, as demonstrated by the results of these studies, was the $HA_6(SA/CS)_4$@VAN/VEGF scaffold. The antibacterial ability of the $HA_6(SA/CS)_4$@VAN/VEGF scaffold was determined using *Staphylococcus aureus* (*S. aureus*). Cytotoxicity, cell adhesion, and osteogenic properties of the $HA_6(SA/CS)_4$@VAN/VEGF scaffold were studied using bone marrow mesenchymal stem cells. The results indicate that the $HA_6(SA/CS)_4$@VAN/VEGF scaffold exhibits good physical, chemical, antibacterial, and osteogenic properties, and is, thus, a new type of bone scaffold composite material with good osteogenic potential.

Keywords: bone regeneration, composite scaffold, drug release, osteogenesis, bone defects, hydroxyapatite, chitosan, sodium alginate

OPEN ACCESS

Edited by:
Ayşen Tezcaner, Middle East Technical University, Turkey

Reviewed by:
Vesna Miskovic-Stankovic, University of Belgrade, Serbia
Giovanni Vozzi, University of Pisa, Italy

***Correspondence:**
Bowei Wang
wangbw@jlu.edu.cn

Specialty section:
This article was submitted to Biomaterials, a section of the journal Frontiers in Materials

Received: *03 January 2021*
Accepted: *23 February 2021*
Published: *18 March 2021*

Citation:
Liu D, Liu Z, Zou J, Li L, Sui X, Wang B, Yang N and Wang B (2021) Synthesis and Characterization of a Hydroxyapatite-Sodium Alginate-Chitosan Scaffold for Bone Regeneration. Front. Mater. 8:648980. doi: 10.3389/fmats.2021.648980

INTRODUCTION

Bone defects are usually caused by trauma, infection, surgery, and diseases, such as osteoporosis and arthritis, and bone tissue replacement is required to rebuild function (Wei et al., 2020). As the body itself cannot repair large bone defects, tissue healing must be promoted through surgical intervention. At present, autologous and allogeneic bone transplantations are the main clinical treatment modalities. However, the risks of secondary infection, immune rejection, donor disease, and limited blood supply need to be circumvented through artificial replacement using bone tissue engineering (Smith et al., 2015; Windhager et al., 2017). Therefore, the development of appropriate

tissue engineering techniques may help circumvent the above shortcomings and accelerate tissue regeneration (Montalbano et al., 2020).

Bone repair is a long-term process, and tissue engineering can be used to promote bone repair. An ideal bone scaffold should have components, structure, and biomechanical properties similar to those of natural bone, serve as a base for bone deposition and provide mechanical support, regulate cell adhesion, proliferation, and differentiation, and provide cells with a microenvironment for osteogenic differentiation (Hao et al., 2017; Kim et al., 2020; Shen et al., 2021). Using bone tissue engineering technology a bone scaffold material carrier can be constructed carrying seed cells and biological factors, and then implanted in the bone defect, to promote bone formation. The development of this new technology eliminates the disadvantages of autogenous and allogeneic bone transplantations. In addition, by adding different biological factors, the process of bone repair can be accelerated and the treatment time can be shortened.

There are two main ways of bone regeneration: intraosseous and cartilage osteogenesis. Among them, osseous osteogenesis is manifested by the direct differentiation of mesenchymal stem cells (MSCs) into osteoblasts. After extracellular matrix secretion, the mineralization is further deposited and the bone defect is finally restored (Loi et al., 2016; Lin et al., 2018). Bone marrow stem cells (BMSCs), which have a great potential to be used as seed cells, play an important role in promoting the regeneration of tissues including bone tissue, skin and blood vessel, nerve tissue, and myocardial tissue (Raynald et al., 2019; Ribeiro et al., 2019; Zhang et al., 2019; Arthur and Gronthos, 2020). BMSCs have become the preferred cell type for bone tissue engineering, and their use has been gradually transferred from the experimental to the clinical stage contributing to obtaining better bone tissue healing outcomes (Hashimoto et al., 2019).

Hydroxyapatite (HA) is the main inorganic component of human bone tissue, showing high biocompatibility, biological activity, and bone formation ability (Koc et al., 2016; Nie et al., 2017; Melo et al., 2020). Furthermore, HA is considered as one of the most promising bone implant materials. However, its high brittleness and low mechanical strength restrict its clinical application. Therefore, HA is often used to form composites with other macromolecules and high-molecular polymers, which can show better bone-forming ability to meet the requirements for ideal bone scaffold materials (Saleem et al., 2020).

Sodium alginate and chitosan are common biological macromolecules (Luo et al., 2018; Arafa et al., 2020). When used with hydroxyapatite, they can promote tissue regeneration and play an important role in bone tissue engineering. However, in current research, these three mixtures are mostly made into hydrogels, bone cements, etc., which are used to promote tissue regeneration and drug delivery (Lima et al., 2020; Zima et al., 2020). The material synthesized by the above preparation method has the disadvantages of low strength, fast degradation rate, single drug-loaded, and so on (Zou et al., 2021). In addition, there are simple microspheres prepared from these three materials for sustained drug release (Bi et al., 2019), but when such microspheres are placed in the body, their position cannot be well-restricted, and they tend to leave the placement area with body fluid circulation and body position changes. Therefore, stent materials with high strength and multiple drug loading can better solve the above-mentioned shortcomings.

Vascular endothelial growth factor (VEGF) is a key physiological angiogenesis regulator in embryonic development and after birth, which can promote the proliferation and migration of endothelial cells and increase the permeability of blood vessels (Uccelli et al., 2019). Current research show that VEGF, in addition to playing an important role in vascular regeneration, also plays an active role in bone regeneration. VEGF plays an important role in different stages of bone tissue repair, including inflammation, endochondral ossification, intramembranous ossification, and bone remodeling in the process of callus formation, and affects the proliferation and differentiation of osteoblasts (Hu and Olsen, 2016). The vascular endothelial growth factor is contained in the scaffold material to promote bone tissue regeneration (Garcia et al., 2016; Chen et al., 2020). At the same time, studies have shown that when sodium alginate is loaded with VEGF, the two are electrostatically combined and will not affect VEGF (Gu et al., 2004). Therefore, VEGF is of great significance for the treatment of bone non-union that is prone to occur in large bone defects.

Bone tissue infection, especially osteomyelitis, is a tricky situation. Therefore, it is necessary to use antibiotics while promoting bone tissue regeneration in order to achieve a good osteogenic effect. Vancomycin (VAN) is widely used clinically as a high-level antibiotic, especially as the antibiotic of choice for methicillin-resistant *S. aureus* (De Vriese and Vandecasteele, 2014). The antibacterial mechanism of vancomycin is to inhibit the peptidoglycan synthesis pathway of the bacterial cell wall (Garcia-Gonzalez et al., 2018). It can be carried in the scaffold and released for a long time to promote bone tissue regeneration without affecting the activity of bone marrow mesenchymal stem cells (Cheng et al., 2018; Yu et al., 2020; He et al., 2021).

Therefore, VAN can be loaded in the scaffold material to achieve a local slow-release of the antibiotic, which is beneficial to the entire osteogenic microenvironment and ultimately promotes bone tissue regeneration. Furthermore, studies have shown that the VAN-loaded scaffold ultimately leads to the formation of a better bone tissue structure (Zhou et al., 2018; Avani et al., 2019).

The aim of this study is to prepare a composite scaffold that possesses an antibacterial action and promotes bone tissue regeneration. We have prepared a stent that can carry two drugs simultaneously, so that the release of the two drugs has a chronological sequence to meet the needs of different stages of bone regeneration. The physical and chemical properties such as swelling, degradation, porosity, and the mechanical properties of the scaffold were evaluated; co-cultivation with BMSCs was also conducted using *in vitro* experiments to evaluate their ability to promote bone tissue regeneration.

EXPERIMENTAL SECTION

Materials and Instruments

The following materials were used in this study: SA, with viscosities of 4–12 and 20 mPa • s (Aldrich Sigma, MO, USA), CS, with a deacetylation degree of 80.00–95.0%, viscosity

of 50–800 mPa • s (Sinopharm Group Chemical Reagent Co., Ltd.), HA (Aldrich Sigma, MO, USA), VAN, with a potency of 906.3 IU (Biosharp, USA), VEGF and its ELISA kit (PeproTech, USA), anhydrous calcium chloride ($CaCl_2$), glacial acetic acid, sodium citrate, no water ethanol, analytically pure (Beijing Chemical Plant), 0.1 mol/L (pH = 7.4) phosphate buffer solution (PBS) (prepared in the laboratory). Healthy specific pathogen free (SPF) grade rats weighing 70–100 g (Liaoning Changsheng Biotechnology Co., Ltd., China), low glucose Dulbecco's Modified Eagle's Medium (L-DMEM), 100 U/mL penicillin, 100 lg/mL streptomycin and 0.25% trypsin (Hyclone, USA), rat bone marrow mesenchymal stem cell medium and mesenchymal stem cells—adipocyte differentiation medium (Sciencell, USA), fetal bovine serum (FBS, BI, Israel), methyl thiazolyl tetrazolium (MTT), β-glycerol phosphate, ascorbic acid and dexamethasone (Sigma, USA), 1% alizarin red S staining solution, oil red O staining solution, BCIP/NBT alkaline phosphatase color development kit, RIPA lysis buffer, phenylmethanesulfonyl fluoride (PMSF), BCA protein assay kit and DAPI staining solution (Beyotime, China), body fluid calcium concentration colorimetric quantitative detection kit (Shanghai Haling Biological Technology Co., Ltd., China), cell total RNA isolation kit (Foregene, China), PrimeScript™ RT reagent Kit with gDNA Erase, primers including alkaline phosphatase (ALP), runx-related transcription factor 2 (RUNX2), bone morphogenetic protein 2 (BMP2) and osteopontin (OCN) and TB Green® Premix Ex Taq™ II RT-PCR (Takara, Japan).

The following instruments were used in this study: ALPHA 1-2LD freeze dryer (Marin Christ, Germany), constant temperature CO_2 incubator (Thermo, USA), automatic microplate reader (Bio-TEX, USA), inverted fluorescence microscope and FV3000 laser confocal microscope (Olympus, Japan), Mx3005P fluorescence quantitative PCR instrument (Stratagene, Japan).

Preparation of Multi-Layer Sustained-Release Microspheres

Preparation of Core Spheres

Core spheres were prepared according to a previously published method (Yang et al., 2015). Briefly, 25 μg of VEGF was dissolved in 20 ml 4% (w/v) SA solution (20 cpSA dissolved in high pressure steam-sterilized deionized water), and stirred evenly to obtain a VEGF-SA solution. Thirty milliliter 15% (w/v) $CaCl_2$ solution (autoclaved) was extracted and put into the beaker. A syringe with a 5 gauge syringe needle was used to suck the VEGF-SA solution, subsequently the solution was dripped into the $CaCl_2$ solution at a uniform speed, and stirred at 300 r/min for 30 min to ensure the SA and Ca^{2+} were fully cross-linked. After the reaction was completed, the residual liquid was suction-filtered, sterilized, and deionized. After washing with water, another suction filtration was performed to obtain the calcium alginate core ball.

Preparation of the Multi-Layer Ball

A total of 30 ml of 1% (w/v) CS acetic acid solution was added in a beaker and stirred at a low speed. The CA core ball prepared in the previous step was added to the CS solution and stirred at 500 r/min for 10 min. The residual liquid was filtered, rinsed with sterile deionized water, and then suction-filtered again to obtain a CA-CS double-layer ball. Thirty milliliters of 0.5% (w/v) sodium alginate solution (4–12 cpSA dissolved in deionized water and sterilized by high pressure steam) was added in a beaker, and stirred at a low speed. The CA-CS double-layer ball prepared in the previous step was added to the above solution, and stirred at 800 r/min for 2 min. The residual liquid was filtered, rinsed with sterile deionized water, and then filtered again to obtain the CA-CS-SA three-layer ball. Next, 30 ml of 1% (w/v) CS acetic acid solution was added in a beaker and stirred at a low speed. The CA-CS-SA three-layer ball prepared in the previous step was added to the CS solution, and stirred at 500 r/min for 10 min. The residual liquid was suction-filtered, rinsed with sterile deionized water and then suction filtered again to obtain the CA-CS-SA-CS four-layer ball. After freeze-drying, the ball was stored at −80°C.

TABLE 1 | The formulations of the scaffolds.

Sample	HA (%)	SA (%)	CS (%)	VEGF	VAN
$HA_0(SA/CS)_{10}$	–	80	20	–	–
$HA_4(SA/CS)_6$	40	48	12	–	–
$HA_5(SA/CS)_5$	50	40	10	–	–
$HA_6(SA/CS)_4$	60	32	8	–	–
$HA_7(SA/CS)_3$	70	24	6	–	–
$HA_0(SA/CS)_{10}$@VEGF/VAN	–	80	20	+	+
$HA_6(SA/CS)_4$@VEGF/VAN	60	32	8	+	+

Preparation of the HA-Reinforced Ball-Bearing Stent

An HA-enhanced ball carrier was prepared with a component ratio of 10% (microsphere volume to total stent volume). According to 6% (w/v) CS acetic acid solution to 2% (w/v) alginic acid, the sodium solution was prepared in a ratio of 1:4, and the SA-CS mixture was prepared by adding 1 mol/L NaOH solution dropwise to adjust the pH to 7.0–7.4. HA was weighed according to the ratio of SA/CS: HA to 6:4, 5:5, 4:6, and 3:7, respectively. The SA/CS/HA mixed solution was prepared by first adding HA weighed in proportion to 1% VAN aqueous solution. The SA/CS solution was added after ultrasonic dispersion for 10 min, and the mixture was stirred at 800 r/min for 30 min. The previously prepared microspheres were added to the mixed solution at a volume ratio of 10%, and stirred at 300 r/min for 10 min. After the microspheres were evenly distributed, the total solution was placed in the mold, kept overnight at −20°C, and then stored at −80°C for 24 h. After freeze-drying, it was soaked in 3% (w/v) $CaCl_2$ for 1 h, rinsed gently with sterile deionized water 3 times, placed again overnight at −20°C, then stored at −80°C for 24 h, and freeze-dried for use. **Table 1** summarizes the formulations of scaffolds.

Characterization

Composition and Internal Structure Analyses

To ensure HA successfully modified SA/CS, we used FTIR spectroscopy to show that HA is present in the composite

scaffold. Four sets of composite scaffolds and raw materials were dried and crushed into powder, and analyzed using FTIR spectroscopy. To further determine the crystal phase of HA in the composite scaffold, we recorded it on a Rigaku D/Max 2550 X-ray diffractometer using X-ray diffraction (XRD), with a scanning speed of 8° min^{-1} and a diffraction angle range of 20°-70°. Transmission electron microscopy (TEM) images were obtained using a Philips Feitner G2STwin microscope, equipped with a field emission gun operating at 200 kV.

Contraction Percentage Measurement

The HA-reinforced ball-bearing stent was fabricated using a 24-hole plate as a mold, and a cylindrical stent. The diameter (d_1) and the height of 1/2 of the diameter of the stent were measured (h_1). The volume of the stent (V_1), and the volume of the stent fluid injected into each hole (V_0) were calculated. Three parallel groups were prepared for each group of samples, and the average value was calculated. The contraction percentage (C) was measured using the following formula: $C = (V_0\text{-}V_1)/V_0 \times 100\%$.

Swelling Behavior

The water absorption and swelling rate of the stent were calculated based on a previous report (Sharmila et al., 2020) and the dry weight (m_0) of the stent was determined. The stent was submerged in PBS in a centrifuge tube. The centrifuge tube of the submerged support was placed in a shaker, and oscillated for 24 h at 37°C, at 60 r/min. Then, it was weighed and three parallel groups were set for each group. The average value was calculated. The swelling rate (S) was determined using the following formula: $S = (m–m_0)/m_0 \times 100\%$.

Mechanical Properties

An electronic universal testing machine was used to measure the compressive elastic modulus of the dry cylindrical support. The temperature was set at 23°C, the constant strain rate was 1 mm/min, and 3 parallel groups were set for each group.

Degradation Studies

The freeze-dried scaffold was weighed (m_0), immersed in a centrifuge tube containing sterile PBS, and placed in a 37°C cell incubator. Every 3 days, it was carefully rinsed three times with sterile deionized water, and weighed m_x after freeze-drying. Three parallel groups were set for each group, and the average value was calculated. Then, the scaffold was submerged again in a centrifuge tube containing sterile PBS. The above steps were repeated for 21 days. The remaining bracket mass fraction (D, %) was calculated using the following formula: $D = m_x/m_0 \times 100\%$.

Porosity Measurement

The absolute porosity of the scaffold material was determined using the liquid ethanol replacement method. V_1 is the initial volume of absolute ethanol in the container. The stent was placed in absolute ethanol for 5 min to ensure that the liquid completely filled the pores. The liquid volume at this stage is called V_2. Then, the stent was removed from the liquid and the volume of the remaining liquid V_3 was determined (Tohamy et al., 2018). The porosity (P) was calculated using the formula: $P = (V_1\text{-}V_3)/(V_2\text{-}V_3) \times 100\%$.

Drug Release Evaluation

The freeze-dried stents were immersed in sterile PBS in centrifuge tubes. VAN was detected on days 1, 2, 3, 4, and 5, and all the sustained-release was removed. The solution was placed at −80°C. VEGF was detected on days 1, 3, 6, 9, 12, and 16. The slow-release solutions were placed at −80°C, and the same amount of sterile PBS was then added to the centrifuge tube. The solution was added to a test tube, three parallel groups were set for each group and the average was calculated. VEGF was detected using an ELISA kit, while VAN was detected using a microplate reader.

Antibacterial Assay

In this study, the gram-positive bacterium *S. aureus* was used to evaluate the antibacterial activity of the scaffold materials. An antibacterial activity test was conducted using a combination of qualitative and quantitative methods. For quantitative analysis, frozen tryptic soy broth (TSB) liquid medium was used to activate frozen *S. aureus* in a 120 r/m shaking incubator. Subsequently, 5 ml of TSB liquid medium was used to transfer the activated *S. aureus* into each centrifuge tube, which was fixed at an OD value of 0.1–0.2 at 625 nm. Then, the TSB medium containing *S. aureus* in each test tube was co-cultured with the HA_6 $(SA/CS)_4$@VAN/VEGF, $HA_6(SA/CS)_4$, $HA_0(SA/CS)_{10}$@VAN/VEGF, and $HA_0(SA/CS)_{10}$ scaffolds, with 4 parallel samples in each group. Subsequently, the mixture was incubated at 37°C for 1, 3, and 5 days, and then the absorbance of each group was monitored using an ultraviolet-visible spectrophotometer at 625 nm.

The antibacterial activity of the stent was observed in the bacteriostatic zone of *S. aureus*. The $HA_6(SA/CS)_4$@VAN/VEGF, $HA_6(SA/CS)_4$, $HA_0(SA/CS)_{10}$@VAN/VEGF, and $HA_0(SA/CS)_{10}$ scaffolds were placed in a 15-mL centrifuge tube; then, 5 ml sterile Ionized water was added, and the scaffolds were incubated at 37°C for 1, 3, and 5 days. Next, *S. aureus* suspended in TSB medium (100 μl) was inoculated onto the agar plate, which was fixed at an OD value of 0.1–0.2 at 625 nm, and then sterile filter paper with a diameter of 6 mm was applied to the plate. A total of 10 μl of the release solution from each group of scaffolds on days 1, 3, and 5 was added dropwise onto sterile filter paper. After incubating at 37°C for 12 h, the diameter of the bacteriostatic ring was measured, photographed, and the sample was stored.

In vitro Studies

Isolation and Culture of BMSCs

The use of Sprague Dawley rats and all related procedures in the following part were approved by Jilin University Stomatology School Animal Care and Use Committee. They were sacrificed by cervical dislocation and immediately immersed in 75% ethanol for 10 min. The bilateral femur and tibia were quickly separated under a sterile environment and immersed in L-DMEM containing 5% penicillin-streptomycin. The attached soft tissue was removed and soaked in another clean L-DMEM containing 5% penicillin-streptomycin. Then, the medullary cavity was exposed by removing the bilateral epiphyseal ends and slowly infused with 5 ml preheated rat bone marrow mesenchymal stem cell medium using a sterile syringe. The

obtained cells were transferred to a 25 cm^2 plastic culture flask for incubation at 37°C in a 5% CO_2 supplemented incubator. After 72 h, the fresh medium was changed and then every 3–4 days.

When the cells at 70–80% confluence, the medium was discarded, rinsed and 0.5 ml 0.25% trypsin was added. The digestion was terminated by adding 3 ml complete culture solution when most cells became spherical. The cell suspension was centrifuged at 1,000 rpm for 5 min, the supernatant was discarded, the cells were resuspended in stem cell medium and subcultured at a 1:2 split ratio. Then, the medium was changed every 3 days until the cells reached 70–80% confluence again. The above passaging process was repeated, and third-generation cells were obtained.

Osteogenic Differentiation of BMSCs

A total of 500 μl of 1% gelatin was used to coat the bottom surface of a 12-well plate for 30 min. Third-generation BMSCs were used to inoculate the gelatin-coated 12-well plate at a density of 5×10^4 cells/well. Cells were divided into a blank group and an induction group, each with 3 multi-wells. After adhering, they were induced with osteogenic induction L-DMEM (L-DMEM, 1% penicillin-streptomycin, 10% FBS, 0.5% 1 mol/L β-glycerol phosphate, 1% 5 mg/mL ascorbic acid, 0.5% 20 nmol/L dexamethasone), and the medium was changed every 3 days. After 11 days, the induction and control groups were rinsed twice with 2 ml PBS, fixed for 10 min with 1 ml 4% paraformaldehyde, rinsed three times with 2 ml deionized water, and avoid 1 ml 1% alizarin red S staining solution. Next, the cells were incubated for 30 min away from the light, rinsed five times with 2 ml deionized water. Images were captured using the inverted microscope.

Adipogenic Differentiation of BMSCs

Third-generation BMSCs were inoculated into a 12-well plate coated with 1% gelatin at a density of 5×10^4 cells/well. Cells were divided into blank and induction groups, respectively, with 3 multiple wells. When the cells reached 90–100% fusion, the cells of induction group were cultured with mesenchymal stem cells-adipocyte differentiation medium and the medium was changed every 4 days. Eleven days later, the medium in the both groups were aspirated and 2 ml PBS was added to rinse twice. Cells were fixed with 1 ml 4% paraformaldehyde for 10 min, rinsed twice with 2 ml deionized water, dipped in 60% isopropyl alcohol for 5 min, incubated with 1 ml of oil red O stain for 20 min in the dark, and rinsed five times with 2 ml of deionized water. Images were obtained using the inverted microscope.

Cytotoxicity Evaluation

Third-generation BMSCs were digested and resuspended separately with complete L-DMEM (L-DMEM containing 10% FBS and 1% penicillin-streptomycin), $HA_0(SA/CS)_{10}$ @VAN/VEGF scaffold extraction and $HA_6(SA/CS)_4$@VAN/VEGF scaffold extraction. They were inoculated into a 96-well plate at 5×10^4 cells/well in three wells of each group of four 96-well plate. The plates were taken out on the first day, third day, fifth day, and seventh day, respectively, 20 μl of 5 mg/mL MTT was added to each well in the dark, and the cells were incubated for 4 h in the incubator. Then, the medium was removed, 150 μl of DMSO solution was added to each well and placed for 10 min on a shaker until the purple crystals were fully melted. The optical density (OD) values were read using an automatic microplate reader at 490 nm.

Determination of Calcium Ion Concentration

Two $HA_0(SA/CS)_{10}$@VAN/VEGF scaffolds and two $HA_6(SA/CS)_4$@VAN/VEGF scaffolds were immersed in 20 ml PBS separately, and placed at 4°C. All the liquid was collected on the first day, the fifth day, the seventh day, and the fourteenth day and fresh 20 ml PBS was added again. After the samples were collected, the concentration calcium ion concentration was determined according to the instruction of the kit for quantitative detection of body fluid calcium ion colorimetry.

Alizarin Red Staining

A total of 500 μl of 1% gelatin was added to a 12-well plate, incubated for 30 min in the ultra-clean bench. Then, the plate was dried for use. Third-generation BMSCs were seeded on a gelatin-coated 12-well plate at a density of 5×10^4 cells/well. Cells were divided into blank, $HA_0(SA/CS)_{10}$@VAN/VEGF, and $HA_6(SA/CS)_4$@VAN/VEGF groups, with three replicate wells per group. When the cells reached 80–90% of confluence, the medium was replaced with the corresponding osteogenic induction medium, that was, blank groups with osteogenic induction L-DMEM, $HA_0(SA/CS)_{10}$@VAN/VEGF groups with $HA_0(SA/CS)_{10}$@VAN/VEGF osteogenic induction medium ($HA_0(SA/CS)_{10}$@VAN/VEGF scaffold extraction, 1% penicillin-streptomycin, 10% FBS, 0.5% 1 mol/L β-glycerol phosphate, 1% 5 mg/mL ascorbic acid, 0.5% 20 nmol/L dexamethasone), $HA_6(SA/CS)_4$@VAN/VEGF groups with $HA_6(SA/CS)_4$@VAN/VEGF osteogenic induction medium ($HA_6(SA/CS)_4$@VAN/VEGF scaffold extraction, 1% penicillin-streptomycin, 10% FBS, 0.5% 1 mol/L β-glycerol phosphate, 1% 5 mg/mL ascorbic acid, 0.5% 20 nmol/L dexamethasone). After 11 days, all samples were treated with an alizarin red staining solution according to the instruction.

ALP Staining

On the eleventh day of osteogenic induction, the medium was aspirated. The cells were rinsed twice with 2 ml PBS, fixed with 1 ml 4% paraformaldehyde for 15 min, and rinsed three times with 2 ml PBS. Then, these cells were stained, observed, and imaged according to the instructions of BCIP/NBT alkaline phosphatase color development kit.

ALP Viability

After osteogenic induction for 11 days, the medium was aspirated and the cells were rinsed twice with 2 ml PBS. A total of 300 μl of RIPA lysis buffer and PMSF was added to lyse cells on ice for 3 min. The cell lysate was collected by centrifugation at 12,000 rpm, at 5°C for 5 min, and then the protein concentration at the supernatant was determined according to the instructions of the BCA protein assay kit. The appropriate ratio was selected to dilute the protein samples, and the ALP kit were followed. The OD values at 405 nm were read using a microplate reader, and the number of DEA enzyme activity units of ALP was calculated.

TABLE 2 | Primer sequences for osteogenesis-related genes for real-time PCR.

Gene	Primer/probe sequence
GAPDH	Forward: 5′-GGCACAGTCAAGGCTGAGAATG-3′
	Reverse: 5′-ATGGTGGTGAAGACGCCAGTA-3′
ALP	Forward: 5′-CAGTGGTATTGTAGGTGCTGTGG-3′
	Reverse: 5′-CCTTTCTGCTTGAGGTTGAGGT-3′
BMP2	Forward: 5′-ACCGTGCTCAGCTTCCATCAC-3′
	Reverse: 5′-CTATTTCCCAAAGCTTCCTGCATTT-3′
OPN	Forward: 5′-GCCGAGGTGATAGCTTGGCTTA-3′
	Reverse: 5′-TTGATAGCCTCATCGGACTCCTG-3′
Runx2	Forward: 5′-CATGGCCGGGAATGATGAG-3′
	Reverse: 5′-TGTGAAGACCGTTATGGTCAAAGTG-3′

Real-Time PCR Analysis

After osteogenic induction for 11 days, the medium was aspirated from each group, and the total RNA was extracted using the cell total RNA isolation kit. Total RNA samples with a purity value of 1.8–2.0 were used to perform reverse transcription to synthesize cDNA with the prime Script™ RT reagent kit with a gDNA eraser. This process adjusts the RNA concentration of each group so that the total RNA amount in the 20 μl reverse transcription system was 1 μg. The cDNA, osteogenic-related gene primers and TB Green® Premix Ex Taq™ II kit were used to prepare a 20 μl reaction system, which was placed in an eight-connected tube, and the PCR reaction was completed in a qRT-PCR instrument. The osteogenic genes analyzed included ALP, bone BMP2, OPN, and Runx2. The primer sequences of each gene are shown in **Table 2**.

Cell Adhesion on the Scaffold

The $HA_6(SA/CS)_4$@VAN/VEGF and $HA_0(SA/CS)_{10}$@VAN/VEGF scaffolds were, respectively, placed in laser confocal dishes, and were pre-wet for 1 h with complete L-DMEM. Third-generation BMSCs were digested and inoculated into scaffolds at 1.0×10^6 cells/scaffold by repeated dropwise addition. After 1 h, the medium was added until the scaffolds were immersed and placed in a CO_2 constant temperature cell incubator. Twenty-four hours later, the medium was discarded, the scaffolds were rinsed twice with pre-warmed PBS, fixed for 10 min with 4% paraformaldehyde, and rinsed twice with PBS again. Then, 0.1% triton X-100 was added to pass through the cell membranes for 5 min, and rinsed twice with PBS again. Next, DAPI staining solution was added to the covering scaffolds for 15 min in the dark, and were rinsed with PBS twice. Finally, cell images were obtained using a laser confocal microscope in the dark.

RESULTS AND DISCUSSION

XRD and FTIR Analyses

Figure 1 shows the FTIR spectrum of HA, SA, CS and composite scaffolds. The peaks detected at 1,091, 1,022, 603, 563, and 960 cm^{-1} correspond to the PO_4^3-band, indicating the presence of the HA phase (Cho et al., 2016; Wijesinghe et al., 2017). The spectrum

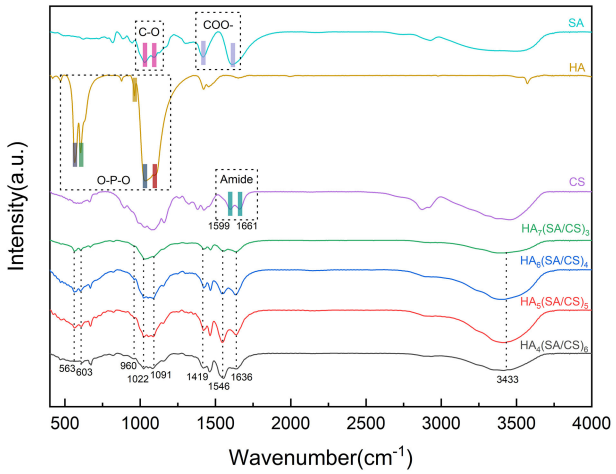

FIGURE 1 | FTIR spectrum of HA, SA, CS, $HA_7(SA/CS)_3$ scaffold, $HA_6(SA/CS)_4$ scaffold, $HA_5(SA/CS)_5$ scaffold, and $HA_4(SA/CS)_6$ scaffold.

of unmodified CS showed characteristic peaks of Amide at 1,661 cm^{-1} (C=O stretching) and 1,599 cm^{-1} (C-N). The vibration peaks of CS at 1,661 and 1,599 cm^{-1} shift to 1,636 and 1,546 cm^{-1} in composite scaffolds. These changes may be attributed to the formation of hydrogen bonding between OH– groups in HA and –C=O groups in CS. For the SA, the absorption peaks at 1,029 and 1,095 cm^{-1} correspond to the stretching vibrations of the C-O. The bands at 1,612 and 1,419 cm^{-1} can be attributed to the symmetric and antisymmetric peaks of the COO- of SA (Sukhodub et al., 2016; You et al., 2019). The band at 3,433 cm^{-1} is due to the interaction between the amide group of CS and the hydroxyl group (Bi et al., 2019). The FTIR spectra of $HA_4(SA/CS)_6$, $HA_5(SA/CS)_5$, $HA_6(SA/CS)_4$, and $HA_7(SA/CS)_3$ tend to be consistent with each other.

To further determine the HA load and the hybrid scaffold, we conducted XRD experiments. The sharp diffraction peaks at $2\theta = 25.8°$, 31.7°, 32.9°, 34.1°, and 45.3° correspond to the faces (002), (211), (300), (202), and (203) of single crystalline HA, respectively. The results shown in **Figure 2**, demonstrate that the diffraction peak position of the composite scaffold group of each ratio is close to the diffraction peak position of the HA particles, and major peaks of HA are in a good agreement with those of HA standard data (JCPDS-09-0432) (Bi et al., 2019; You et al., 2019). The difference between the peaks may be due to the low crystallinity of HA caused by the synthesis of scaffolds and the different amount of HA in different scaffolds. It shows that during the preparation of the composite scaffold, the HA was successfully incorporated into the scaffolds. The CS acetic acid solution is slightly acidic, and in an acidic environment, the dissolved structure of HA changes. We constantly tried to adjust the PH method to avoid white flocs due to too fast adjustment of the PH, and finally the mixture was adjusted to a neutral environment. The FTIR and XRD results confirmed that the HA crystal structure was not damaged, and that it was perfectly mixed inside the stent.

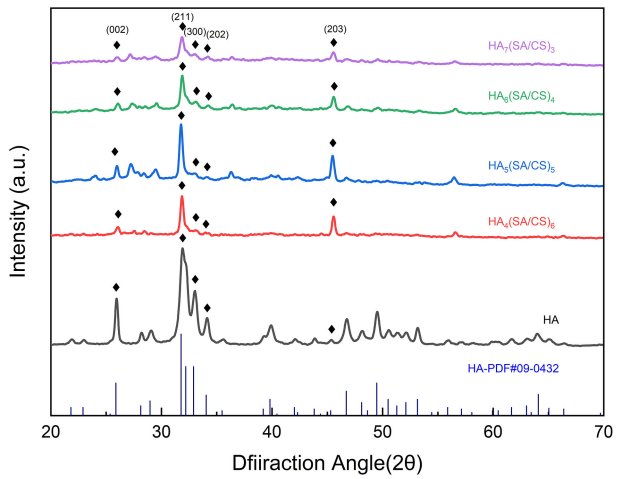

FIGURE 2 | XRD spectrum of HA, $HA_7(SA/CS)_3$ scaffold, $HA_6(SA/CS)_4$ scaffold, $HA_5(SA/CS)_5$ scaffold, and $HA_4(SA/CS)_6$ scaffold.

Scanning Electron Microscope (SEM) Analysis

The interior of the stent is crucial for the "microenvironment." The size of the pores and the connectivity between them affect cell adhesion and crawling, the exchange between nutrients and metabolic waste, blood vessels, and bone regeneration (Peter et al., 2010; He et al., 2019). As shown in **Figure 3**, the pores in each group of stents are connected to each other in a mesh-like structure. Observation under the microscope shows that as the increasing proportion of HA added, the pore size and pore number in the stent become negatively correlated. The $HA_4(SA/CS)_6$ sets of stents are loose and porous, and the pore size can be up to 500 μm, whereas the $HA_5(SA/CS)_5$ and $HA_6(SA/CS)_4$ sets of stents have an internal pore size of 100–300 μm. The $HA_7(SA/CS)_3$ sets of stents are relatively dense and the pore size is only about 100 μm. The difference in pore size among the four groups of stents is obvious. Hence the stents that are beneficial to bone tissue regeneration can be selected based on pore size. Studies have shown that scaffolds with a pore size of 100–200 μm have obvious osteogenic effects *in vitro* (Brennan et al., 2019), and stents with a pore size of about 133 μm are conducive to the production of extracellular matrix *in vitro* (Lutzweiler et al., 2019). However, studies by Oh et al. (2007) have shown that in *in vivo* experiments scaffolds of 290–310 μm are more suitable for the formation of new bones. In addition, Roosa et al. (2010) also found that scaffolds with pore diameter of 350–800 μm can show bone tissue growing outside the scaffold, but scaffolds with pore diameter <350 μm show obvious in stent bone formation.

Contraction Percentage Test

In stents made of multiple phases, CS can reduce the shrinkage performance of the stent (Peng et al., 2016), which is beneficial to the formation of the stent and has the ability to prevent deformation. In the experimental group, the contraction percentage of the stent was positively correlated with the specific gravity of HA, and its contraction percentage performance was more obvious in the vertical height. HA further compresses the space in the height direction of the stent due to its large specific gravity. In **Figure 4A**, in the $HA_4(SA/CS)_6$ and $HA_5(SA/CS)_5$ stent groups, the contraction percentage was significantly lower than that of the control group. However, as the proportion of HA continues to increase, it exerts a more significant effect on the overall stability of the interior of the stent. It plays a role of "load-bearing wall" in maintaining the height of the scaffold, and finally shows higher dimensional stability in the high proportion group. The gravity of hydroxyapatite determines the anisotropy of scaffold contraction.

Swelling Behavior

HA has a large specific gravity and strong hydrophilicity (Januariyasa et al., 2020). When the proportion of HA in the stent is small, the hydrophilic capacity of the stent can be increased, and finally the stent shows water swelling. However, when the specific gravity of medium HA gradually increases, the gravity factor is more important than the hydrophilic factor for the stent's water absorption and swelling ability. This is demonstrated in **Figure 4B**, in which a gradual decrease of the water absorption and swelling ability of the stent is observed. In the scanning electron micrograph, HA is uniformly dispersed in the scaffold, and after crosslinking, it binds firmly with SA and CS. Slight water absorption and swelling can fill the small gap between the scaffold and the bone defect, which is conducive to the adhesion and migration of cells at the interface between the scaffold and the bone tissue, and ensures that the cells enter the scaffold to form bone inside it.

Mechanical Properties

Figure 4C shows the elastic modulus of the composite scaffold with different weight ratios of HA/SA/CS. It can be seen that after adding HA, the mechanical strength of the composite scaffold is positively correlated with the specific gravity of the HA. This is consistent with other reports (Chen et al., 2019; Mondal et al., 2020). The mechanical strength of $HA_7(SA/CS)_3$ stent group was more than 6 times that of $HA_0(SA/CS)_{10}$. The scanning electron microscope showed that the interior of the stent with the high proportion of HA is denser. This is because HA can be embedded in the wall of the stent hole, which increases the strength of the composite stent, but as the proportion of HA increases, the proportion of SA and CS decreases, and the brittleness of the composite stent increases significantly.

Degradation Studies

The degradation rate of the scaffold at the bone defect should ideally match the speed of new bone formation. The rate of bone tissue regeneration is much slower than that of soft tissue regeneration (Peñarrocha-Diago et al., 2020). Thus, if the scaffold degrades rapidly during the early stage of bone formation, it will not provide a good barrier for bone tissue regeneration, and this will ultimately lead to soft tissue expansion into the bone defect, which is not conducive to bone organizational regeneration. As shown in **Figure 4D**, the degradation rate of the $HA_4(SA/CS)_6$

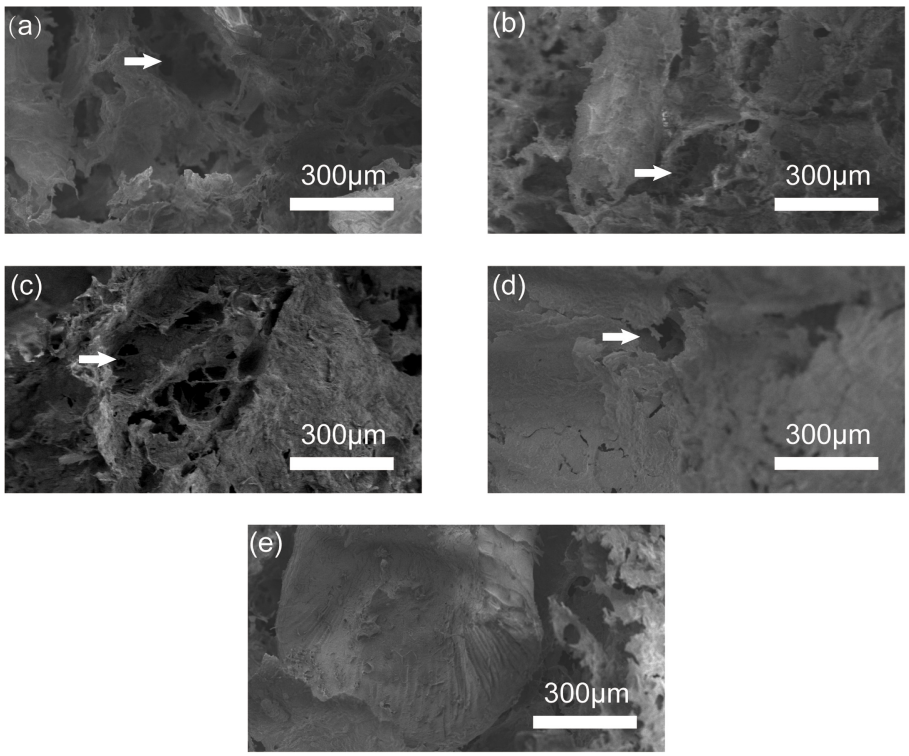

FIGURE 3 | SEM image of **(a)** $HA_4(SA/CS)_6$ scaffold, **(b)** $HA_5(SA/CS)_5$ scaffold, **(c)** $HA_6(SA/CS)_4$ scaffold, **(d)** $HA_7(SA/CS)_3$ scaffold, and **(e)** microsphere inside the scaffold.

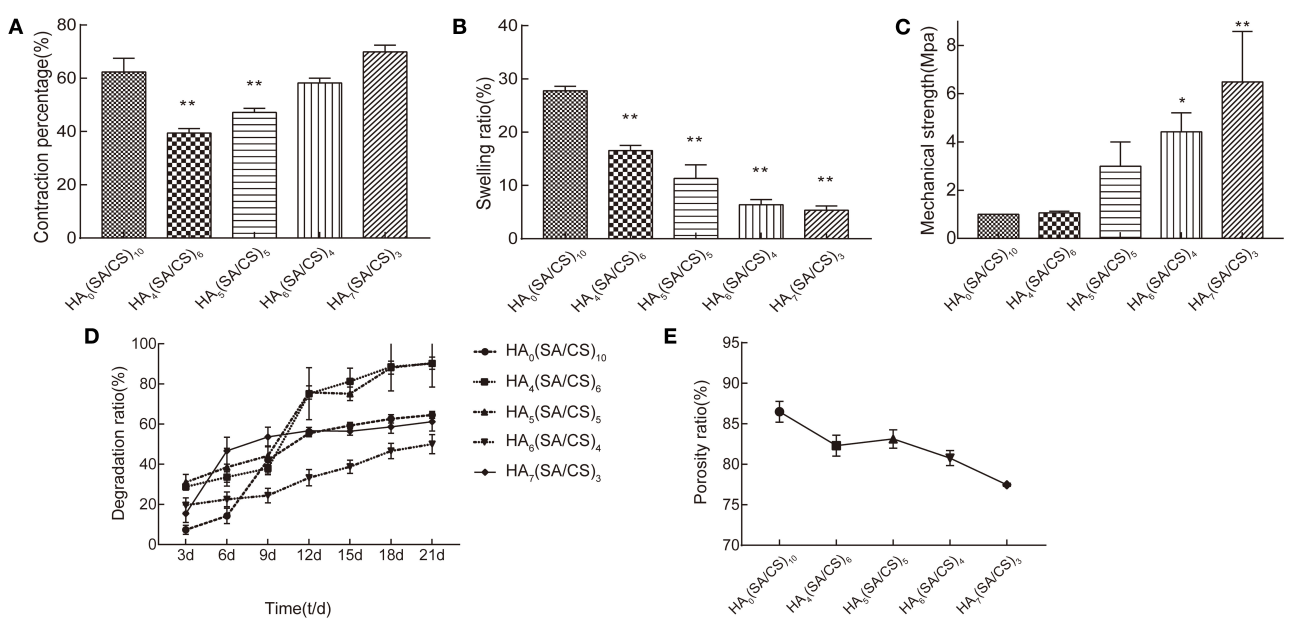

FIGURE 4 | (A) Contraction percentage, **(B)** swelling ratio, **(C)** mechanical strength, **(D)** degradation ratio, **(E)** porosity ratio of $HA_0(SA/CS)_{10}$ scaffold, $HA_4(SA/CS)_6$ scaffold, $HA_5(SA/CS)_5$ scaffold, $HA_6(SA/CS)_4$ scaffold, and $HA_7(SA/CS)_3$ scaffold. $^*p < 0.05$, $^{**}p < 0.01$.

and $HA_5(SA/CS)_5$ scaffold group was the fastest, reaching a degradation rate of 90% on day 21, whereas the degradation rate of the $HA_6(SA/CS)_4$ scaffold group was relatively stable, being 50.01% on day 21. In $HA_7(SA/CS)_3$ scaffold group, the degradation amount accounted for 31.29% of the total stent from the 3rd to the 6th day, and then the degradation tended

to be gentle. This occurs because the water-swelling expansion force of the slow-release microspheres encased in the scaffold is much greater than that in $HA_7(SA/CS)_3$. The specific gravity of sodium alginate chitosan in $HA_7(SA/CS)_3$ scaffold group was lower than that in $HA_6(SA/CS)_4$ scaffold group, which led to the stent rupture from the inside, and a part of sustained-release microspheres were separated from the stent, resulting in a significant reduction in weight. The microspheres detached from the inside of the support, resulting in a significant reduction in weight.

Porosity Measurement

A higher porosity can ensure a higher material exchange capacity inside the stent, which is conducive to maintaining the steady state of the "osteogenesis microenvironment" (Shi et al., 2007). The increase of HA compresses the volume of the scaffold at the height level, resulting in a decrease in the porosity of the scaffold in the experimental group. Furthermore, the cross-linking of the calcium chloride solution establishes a large number of connections between SA and CS (Heo et al., 2017). The stent pores are further reduced and stabilized. As shown in **Figure 4E**, the porosity of the $HA_4(SA/CS)_6$, $HA_5(SA/CS)_5$, and $HA_6(SA/CS)_4$ scaffold groups can reach 80%, and the porosity of the $HA_7(SA/CS)_3$ scaffold group can decrease to 77.47%. Therefore, the $HA_5(SA/CS)_5$ and $HA_6(SA/CS)_4$ sets of scaffolds are more conducive to the formation of bone tissue inside them.

Scaffold Drug Release Ability

The composite stent prepared in this experiment carried two drugs, VEGF and VAN. VEGF was wrapped in internal microspheres and VAN was carried in an external stent. As shown in **Figure 5**, the release curve of the two different stents was not significantly different due to the uniform mixing of the VAN in the external stent. Furthermore, the released amount reached 80% on day 4, demonstrating that a higher concentration of VAN is maintained during early bone defect regeneration, inhibiting the growth of bacteria in the bone defect, and providing a bacteria-free environment during the early stages of bone regeneration (Zhou et al., 2018; Wei et al., 2019). In the early stage of drug release, due to the presence of the SA-CS block layer outside the slow-release microspheres inside the stent, the early release of VEGF was small. As the stent degraded, the VEGF inside the microspheres was gradually released. The release of VEGF in the $HA_6(SA/CS)_4$@VEGF/VAN stent was greater than that of the $HA_0(SA/CS)_{10}$@VEGF/VAN stent from day 6 to day 9, which is related to the good hydrophilicity of HA (Babaei et al., 2019). Since day 9, the release of VEGF tended to be flat.

Detection of Stent Antibacterial Properties

The quantitative and qualitative antibacterial experiments showed that the composite stent had good antibacterial properties. As shown in **Figure 6**, the $HA_6(SA/CS)_4$@VEGF/VAN scaffold and the $HA_0(SA/CS)_{10}$@VEGF/VAN scaffold showed obvious antibacterial ability. Because of the lack of effective antibacterial ingredients, the $HA_6(SA/CS)_4$@VEGF and $HA_0(SA/CS)_{10}$@VEGF scaffolds showed no obvious growth inhibitory effect on *S. aureus*. Obviously, on the first day, the VAN (+) stent showed a good antibacterial performance, and maintained a stable antibacterial effect on days 3 and 5. As shown in the figure, after 1, 3, and 5 days of incubation, a clear inhibitory ring was formed around the $HA_6(SA/CS)_4$@VEGF/VAN and $HA_0(SA/CS)_{10}$@VEGF/VAN scaffolds, which indicates that the VAN released by the scaffold has biological activity. Each antibacterial ring uses a vernier caliper to measure the diameter every 60°, that is, each antibacterial ring is measured three times. The results show that the VAN (+) bracket has a good antibacterial property. The release of active VAN could inhibit the bacteria in the bone defect and prevent the slow or even poor healing of bone tissue caused by the presence of bacteria (Avani et al., 2019; Wei et al., 2019).

BMSCs Morphology and Growth Status

After 72 h of standing culture, several clone colonies of primary BMSCs were seen, which primarily composed of astrocytes, with a small number of spindle cells, and a large number of blood cells and other miscellaneous cells, as shown in **Figure 7a**. Though continuous passage, the astrocytes were elongated, mainly fusiform, arranged in a vortex-like growth, with fewer heterocells and higher purity, as shown in **Figures 7b,c**.

BMSCs Differentiation Test

After 11 days of osteoinduction, alizarin red staining showed obvious calcium nodules, as shown in **Figure 7d**. After 7 days of induction of fat formation, tiny lipid droplets could be seen in the cells under the microscope. With the extension of the induction time, the lipid droplets gradually became larger and merged. Eleven days later, oil red O staining showed obvious lipid droplets, as shown in **Figure 7e**.

Cytotoxicity Test

Figure 7f shows that the cells were co-cultured with complete L-DMEM and scaffold extraction separately. On days 1, 3, 5, and 7, the cells in the blank group, $HA_0(SA/CS)_{10}$@VEGF/VAN group, and $HA_6(SA/CS)_4$@VEGF/VAN group all showed good proliferation ability. There was no statistically significant difference in cell proliferation among the three groups. Compared with the blank, the $HA_0(SA/CS)_{10}$@VEGF/VAN and $HA_6(SA/CS)_4$@VEGF/VAN groups were not cytotoxic, which was conducive to cell adhesion in the scaffold.

Effect of the HA/SA/CS Scaffold on Osteogenic Differentiation of BMSCs

Calcium Ion Release

On days 1, 5, 7, and 14, the $HA_6(SA/CS)_4$@VEGF/VAN and $HA_0(SA/CS)_{10}$@VEGF/VAN scaffolds released calcium ions in PBS as shown in **Figure 7g**. Within 14 days, the two groups of stents continued to release calcium ions, but there was no statistical difference in the released amount. With the degradation, the release of calcium ion in hydroxyapatite is relatively slow (Witek et al., 2017). In addition, $CaCl_2$ solution was used for cross-linking during the preparation of scaffolds, which made sodium alginate become calcium alginate. Over time, calcium ion release in calcium alginate was relatively large, so

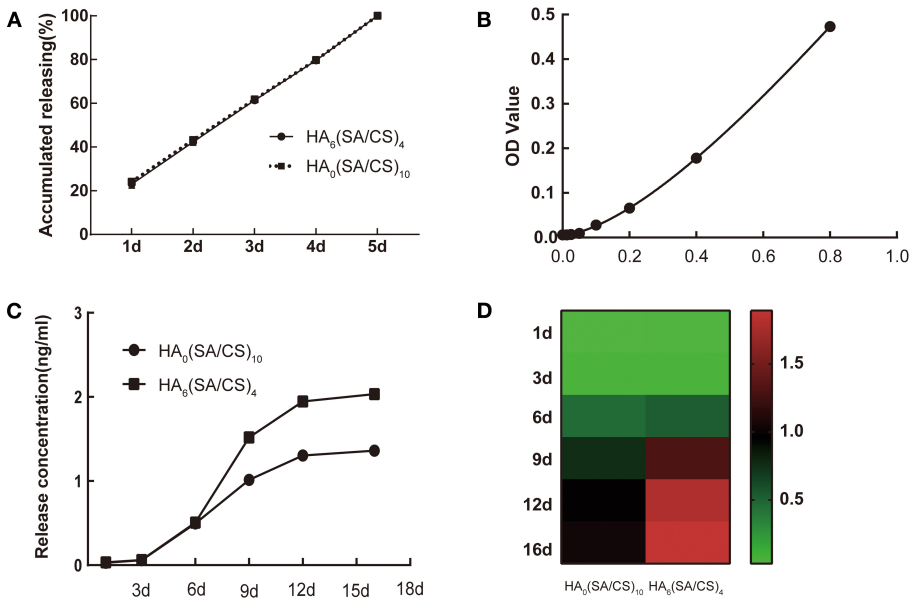

FIGURE 5 | (A) The release curve of VAN on $HA_0(SA/CS)_{10}$ scaffold and $HA_6(SA/CS)_4$ scaffold. **(B)** A standard ELISA curve for VEGF. **(C)** The VEGF release curves of $HA_0(SA/CS)_{10}$ scaffold and $HA_6(SA/CS)_4$ scaffold. **(D)** The VEGF release of heat map of $HA_0(SA/CS)_{10}$ scaffold and $HA_6(SA/CS)_4$ scaffold.

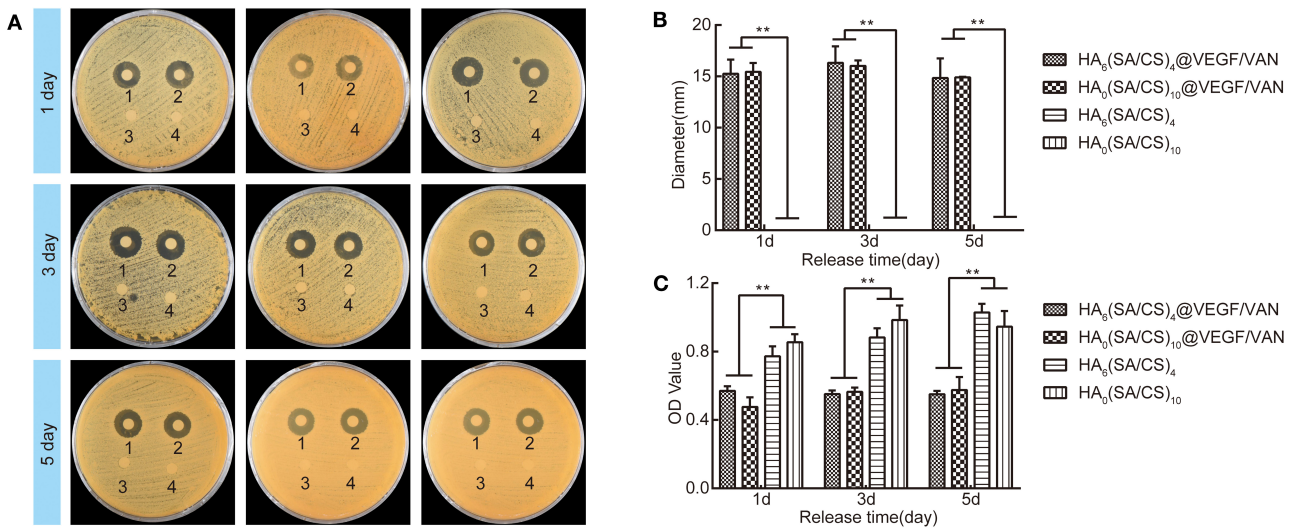

FIGURE 6 | (A) Bacterial growth inhibition on agar plates after 1d, 3d, and 5d. **(B)** The diameter of bacteriostatic rings of the four groups of scaffolds cultured for 1d, 3d, and 5d. **(C)** The OD value of the bacterial liquid medium after the scaffold and the bacterial liquid medium were co-cultured for 1d, 3d, and 5d. Numbers 1–4 indicate $HA_0(SA/CS)_{10}$@VEGF/VAN scaffold, $HA_6(SA/CS)_4$@VEGF/VAN scaffold, $HA_0(SA/CS)_{10}$ scaffold, and $HA_6(SA/CS)_4$ scaffold. $^{**}p < 0.01$.

there was no significant difference in calcium ion release between the two groups.

Calcium ions play an important role in the process of bone reconstruction. A low extracellular concentration of calcium ions (2–4 mm) can affect the calcium-sensitive receptor of osteoblasts, leading to the activation of the intracellular mechanism, increasing the expression of insulin-like growth factor, and promoting the survival and proliferation of osteoblasts. Furthermore, a moderate concentration of calcium ion (6–8 mm) can promote the differentiation of osteoblasts. When the concentration of calcium ions is higher than 10 mm, it will affect the health of osteoblasts (Maeno et al., 2005; Shie and Ding, 2013).

Degree of Mineralization of the Extracellular Matrix

After 11 days of osteogenic induction, the alizarin red staining results were shown in **Figures 8a–c**. The three groups had different degrees of calcium salt deposition. The number of

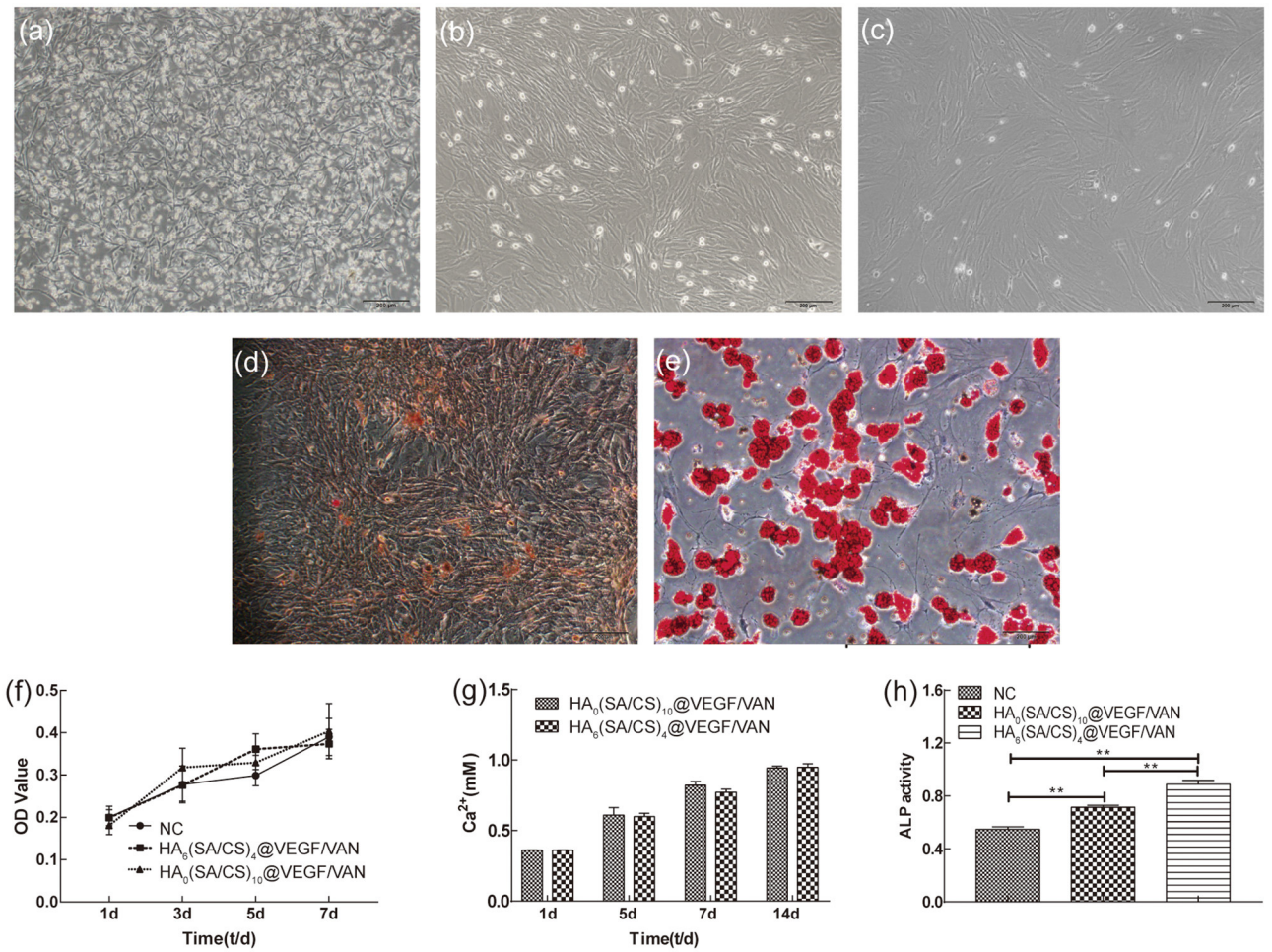

FIGURE 7 | (a) Morphology of primary BMSCs. **(b)** Morphology of first generation BMSCs. **(c)** Morphology of third generation BMSCs. **(d)** Alizarin red staining showed calcium nodules. **(e)** Oil red O staining showed lipid droplets. **(f)** Cytotoxicity test of blank group, $HA_0(SA/CS)_{10}$@VEGF/VAN scaffold and $HA_6(SA/CS)_4$@VEGF/VAN scaffold. **(g)** Ca^{2+} released from the scaffolds. **(h)** Results of ALP activity measurement in each group. $^{**}p < 0.01$.

scaffolds was more than that of the blank group, and the $HA_6(SA/CS)_4$@VEGF/VAN group was obviously more than $HA_0(SA/CS)_{10}$@VEGF/VAN group.

Cell ALP Activity and Expression Levels

The results of ALP activity were shown in **Figure 8**. The staining results showed that the staining in **Figure 8d** was the lightest, while that in **Figure 8f** was the strongest. The degree of staining directly reflected the level of ALP expression, indicating that the expression level of the blank group was the lowest and the expression level of the $HA_6(SA/CS)_4$@VEGF/VAN group was the highest. The results of ALP semi-quantitative analysis, in **Figure 7h**, showed that the DEA enzyme activity of the ALP in the scaffold groups was significantly higher than that in the blank group. Compared with the $HA_0(SA/CS)_{10}$@VEGF/VAN group, the $HA_6(SA/CS)_4$@VEGF/VAN group had a statistically higher expression of ALP.

Cell Adhesion on the Scaffold

The results of layered scanning of the stent material were shown in **Figures 9a,b**. The round blue-stained structures were the nuclei, which indicated that the cells attached successfully to the three-dimensional structure of the $HA_0(SA/CS)_{10}$@VEGF/VAN and $HA_6(SA/CS)_4$@VEGF/VAN scaffolds. As for the number of cells, cells adhered inside the $HA_6(SA/CS)_4$@VEGF/VAN scaffold were significantly higher than that of $HA_0(SA/CS)_{10}$@VEGF/VAN scaffold.

Transcription Levels of Osteogenesis Related Genes

As shown in **Figure 9c**, compared with the blank control group, the expression levels of BMP2 and OPN in the $HA_0(SA/CS)_{10}$@VEGF/VAN group were statistically different, while the expression levels of ALP, BMP2, OPN, and Runx2 in the $HA_6(SA/CS)_4$@VEGF/VAN group were different. The expression levels of ALP, BMP2, OPN and Runx2 were compared between the $HA_0(SA/CS)_{10}$@VEGF/VAN and $HA_6(SA/CS)_4$@VEGF/VAN groups. ALP is a marker of

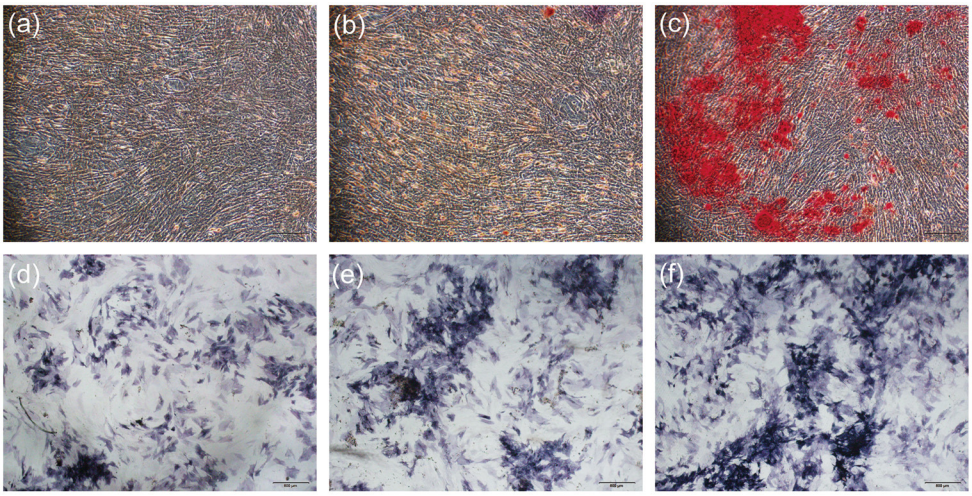

FIGURE 8 | (a) Alizarin red staining of blank group. **(b)** Alizarin red staining of $HA_0(SA/CS)_{10}$@VEGF/VAN scaffold. **(c)** Alizarin red staining of $HA_6(SA/CS)_4$@VEGF/VAN scaffold. **(d)** Results of intracellular ALP activity expression in blank group. **(e)** Results of intracellular ALP activity expression in $HA_0(SA/CS)_{10}$@VEGF/VAN scaffold. **(f)** Results of intracellular ALP activity expression in $HA_6(SA/CS)_4$@VEGF/VAN scaffold.

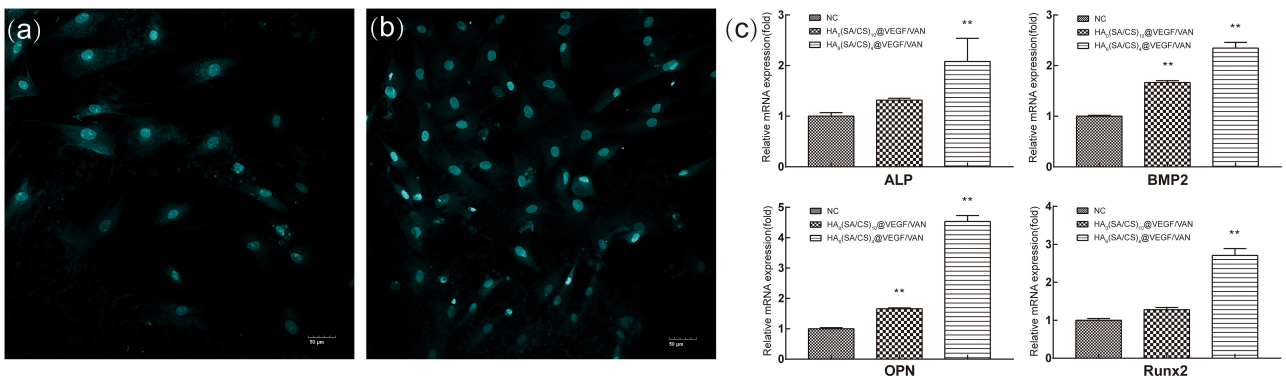

FIGURE 9 | (a) Laser confocal image of cells adhesion on $HA_0(SA/CS)_{10}$@VEGF/VAN scaffold. **(b)** Laser confocal image of cells adhesion on. **(c)** Real-time PCR results of osteogenesis-related gene in each group. $^{**}p < 0.01$.

osteoblasts in the early stage of maturation, while Runx2 is another marker of osteoblasts in the early stage of maturation, which participates in all stages of stem cell differentiation into mature osteoblasts (Bruderer et al., 2014). OPN is a marker of the final stage of osteoblast differentiation, which plays a role in the mineralization of the extracellular matrix and the adhesion between osteoblasts and the matrix. BMP 2 can regulate ALP, Runx2, OPN, and other osteoblasts through different signal pathways. The orderly expression of related genes ALP, Runx2, OCN, and BMP2 is involved in the process of bone formation and bone metabolism, and their transcriptional expression level reflects to a great extent the degree of osteogenic differentiation of BMSCs. Real-time PCR results showed that osteogenic genes in BMSCs were activated and expressed in varying degrees after osteogenic induction. Compared with $HA_0(SA/CS)_{10}$@VEGF/VAN scaffolds, $HA_6(SA/CS)_4$@VEGF/VAN scaffolds had more significant effects on ALP, BMP2, OPN, and Runx2 expression.

CONCLUSION

We successfully prepared and used a SA/CS/HA composite scaffold loaded with VEGF and VAN. By synthesizing composite scaffolds with different ratios and conducting performance tests, we selected the composite scaffolds with the best performance. Hence, the chronological release of the two drugs and the mechanical strength of the scaffold are guaranteed. The composite scaffold has good performance and provides a new strategy for repairing bone defects in infected areas.

DATA AVAILABILITY STATEMENT

The raw data supporting the conclusions of this article will be made available by the authors, without undue reservation.

ETHICS STATEMENT

The animal study was reviewed and approved by Jilin University Stomatology School Animal Care and Use Committee.

AUTHOR CONTRIBUTIONS

BoW and DL designed the work. DL and ZL wrote the manuscript. DL, JZ, LL, and XS carried out the experiments. DL, BiW, and NY carried out the literature search, data acquisition, and data analysis. All authors have read and approved the content of the manuscript.

FUNDING

This study was supported by the Key Scientific and Technological Research and Development Projects (20180201056YY), and the Medical and Health Project (20190304032YY) of the Science and Technology Department of Jilin province of China, and Graduate Innovation Fund of Jilin University (101832018C082).

REFERENCES

Arafa, M. G., Mousa, H. A., and Afifi, N. N. (2020). Preparation of PLGA-chitosan based nanocarriers for enhancing antibacterial effect of ciprofloxacin in root canal infection. *Drug Deliv.* 27, 26–39. doi: 10.1080/10717544.2019.1701140

Arthur, A., and Gronthos, S. (2020). Clinical application of bone marrow mesenchymal stem/stromal cells to repair skeletal tissue. *Int. J. Mol. Sci.* 21:9759. doi: 10.3390/ijms21249759

Avani, F., Damoogh, S., Mottaghitalab, F., Karkhaneh, A., and Farokhi, M. (2019). Vancomycin loaded halloysite nanotubes embedded in silk fibroin hydrogel applicable for bone tissue engineering. *Int. J. Polym. Mater. Poly.* 69, 32–43. doi: 10.1080/00914037.2019.1616201

Babaei, M., Ghaee, A., and Nourmohammadi, J. (2019). Poly (sodium 4-styrene sulfonate)-modified hydroxyapatite nanoparticles in zein-based scaffold as a drug carrier for vancomycin. *Mater. Sci. Eng. C Mater. Biol. Appl.* 100, 874–885. doi: 10.1016/j.msec.2019.03.055

Bi, Y. G., Lin, Z. T., and Deng, S. T. (2019). Fabrication and characterization of hydroxyapatite/sodium alginate/chitosan composite microspheres for drug delivery and bone tissue engineering. *Mater. Sci. Eng. C Mater. Biol. Appl.* 100, 576–583. doi: 10.1016/j.msec.2019.03.040

Brennan, C., Eichholz, K., and Hoey, D. (2019). The effect of pore size within fibrous scaffolds fabricated using melt electrowriting on human bone marrow stem cell osteogenesis. *Biomed. Mater.* 14:065016. doi: 10.1088/1748-605X/ab49f2

Bruderer, M., Richards, R. G., Alini, M., and Stoddart, M. J. (2014). Role and regulation of RUNX2 in osteogenesis. *Eur. Cell. Mater.* 28, 269–286. doi: 10.22203/eCM.v028a19

Chen, C. Y., Chen, C. C., Wang, C. Y., Lee, A. K., Yeh, C. L., and Lin, C. P. (2020). Assessment of the release of vascular endothelial growth factor from 3D-printed poly-epsilon-caprolactone/hydroxyapatite/calcium sulfate scaffold with enhanced osteogenic capacity. *Polymers* 12:1455. doi: 10.3390/polym12071455

Chen, S., Shi, Y., Zhang, X., and Ma, J. (2019). 3D printed hydroxyapatite composite scaffolds with enhanced mechanical properties. *Ceram. Int.* 45, 10991–10996. doi: 10.1016/j.ceramint.2019.02.182

Cheng, T., Qu, H., Zhang, G., and Zhang, X. (2018). Osteogenic and antibacterial properties of vancomycin-laden mesoporous bioglass/PLGA composite scaffolds for bone regeneration in infected bone defects. *Artif. Cells Nanomed. Biotechnol.* 46, 1935–1947. doi: 10.1080/21691401.2017.1396997

Cho, J. S., Lee, J. C., and Rhee, S. H. (2016). Effect of precursor concentration and spray pyrolysis temperature upon hydroxyapatite particle size and density. *J. Biomed. Mater. Res. Part B Appl. Biomater.* 104, 422–430. doi: 10.1002/jbm.b.33406

De Vriese, A. S., and Vandecasteele, S. J. (2014). Vancomycin: the tale of the vanquisher and the pyrrhic victory. *Perit. Dial. Int.* 34, 154–161. doi: 10.3747/pdi.2014.00001

Garcia, J. R., Clark, A. Y., and Garcia, A. J. (2016). Integrin-specific hydrogels functionalized with VEGF for vascularization and bone regeneration of critical-size bone defects. *J. Biomed. Mater. Res. A* 104, 889–900. doi: 10.1002/jbm.a.35626

Garcia-Gonzalez, C. A., Barros, J., Rey-Rico, A., Redondo, P., Gomez-Amoza, J. L., Concheiro, A., et al. (2018). Antimicrobial properties and osteogenicity of vancomycin-loaded synthetic scaffolds obtained by supercritical foaming. *ACS Appl. Mater. Interfaces* 10, 3349–3360. doi: 10.1021/acsami.7b17375

Gu, F., Amsden, B., and Neufeld, R. (2004). Sustained delivery of vascular endothelial growth factor with alginate beads. *J. Control. Release* 96, 463–472. doi: 10.1016/j.jconrel.2004.02.021

Hao, Z., Song, Z., Huang, J., Huang, K., Panetta, A., Gu, Z., et al. (2017). The scaffold microenvironment for stem cell based bone tissue engineering. *Biomater. Sci.* 5, 1382–1392. doi: 10.1039/C7BM00146K

Hashimoto, Y., Nishida, Y., Takahashi, S., Nakamura, H., Mera, H., Kashiwa, K., et al. (2019). Transplantation of autologous bone marrow-derived mesenchymal stem cells under arthroscopic surgery with microfracture versus microfracture alone for articular cartilage lesions in the knee: a multicenter prospective randomized control clinical trial. *Regen. Ther.* 11, 106–113. doi: 10.1016/j.reth.2019.06.002

He, J., Hu, X., Cao, J., Zhang, Y., Xiao, J., Peng, L., et al. (2021). Chitosan-coated hydroxyapatite and drug-loaded polytrimethylene carbonate/polylactic acid scaffold for enhancing bone regeneration. *Carbohydr. Polym.* 253:117198. doi: 10.1016/j.carbpol.2020.117198

He, X., Liu, Y., Tan, Y., Grover, L. M., Song, J., Duan, S., et al. (2019). Rubidium-containing mesoporous bioactive glass scaffolds support angiogenesis, osteogenesis and antibacterial activity. *Mater. Sci. Eng. C Mater. Biol. Appl.* 105:110155. doi: 10.1016/j.msec.2019.110155

Heo, E. Y., Ko, N. R., Bae, M. S., Lee, S. J., Choi, B.-J., Kim, J. H., et al. (2017). Novel 3D printed alginate–BFP1 hybrid scaffolds for enhanced bone regeneration. *J. Ind. Eng. Chem.* 45, 61–67. doi: 10.1016/j.jiec.2016.09.003

Hu, K., and Olsen, B. R. (2016). The roles of vascular endothelial growth factor in bone repair and regeneration. *Bone* 91, 30–38. doi: 10.1016/j.bone.2016.06.013

Januariyasa, I. K., Ana, I. D., and Yusuf, Y. (2020). Nanofibrous poly(vinyl alcohol)/chitosan contained carbonated hydroxyapatite nanoparticles scaffold for bone tissue engineering. *Mater. Sci. Eng. C Mater. Biol. Appl.* 107:110347. doi: 10.1016/j.msec.2019.110347

Kim, H. D., Park, J., Amirthalingam, S., Jayakumar, R., and Hwang, N. S. (2020). Bioinspired inorganic nanoparticles and vascular factor microenvironment directed neo-bone formation. *Biomater. Sci.* 8, 2627–2637. doi: 10.1039/D0BM00041H

Koc, A., Elcin, A. E., and Elcin, Y. M. (2016). Ectopic osteogenic tissue formation by MC3T3-E1 cell-laden chitosan/hydroxyapatite composite scaffold. *Artif. Cell Nanomed. Biotechnol.* 44, 1440–1447. doi: 10.3109/21691401.2015.1036998

Lima, D. B., De Souza, M., a,.A., De Lima, G. G., Ferreira Souto, E. P., Oliveira, H.M. L., et al. (2020). Injectable bone substitute based on chitosan with polyethylene glycol polymeric solution and biphasic

calcium phosphate microspheres. *Carbohydr. Polym.* 245:116575. doi: 10.1016/j.carbpol.2020.116575

Lin, X., Zhao, C., Zhu, P., Chen, J., Yu, H., Cai, Y., et al. (2018). Periosteum extracellular-matrix-mediated acellular mineralization during bone formation. *Adv. Healthc. Mater.* 7:1700660. doi: 10.1002/adhm.201700660

Loi, F., Cordova, L. A., Pajarinen, J., Lin, T. H., Yao, Z., and Goodman, S. B. (2016). Inflammation, fracture and bone repair. *Bone* 86, 119–130. doi: 10.1016/j.bone.2016.02.020

Luo, Y., Li, Y., Qin, X., and Wa, Q. (2018). 3D printing of concentrated alginate/gelatin scaffolds with homogeneous nano apatite coating for bone tissue engineering. *Mater. Design* 146, 12–19. doi: 10.1016/j.matdes.2018.03.002

Lutzweiler, G., Barthes, J., Koenig, G., Kerdjoudj, H., Mayingi, J., Boulmedais, F., et al. (2019). Modulation of cellular colonization of porous polyurethane scaffolds via the control of pore interconnection size and nanoscale surface modifications. *ACS Appl. Mater. Interfaces* 11, 19819–19829. doi: 10.1021/acsami.9b04625

Maeno, S., Niki, Y., Matsumoto, H., Morioka, H., Yatabe, T., Funayama, A., et al. (2005). The effect of calcium ion concentration on osteoblast viability, proliferation and differentiation in monolayer and 3D culture. *Biomaterials* 26, 4847–4855. doi: 10.1016/j.biomaterials.2005.01.006

Melo, P., Naseem, R., Corvaglia, I., Montalbano, G., Pontremoli, C., Azevedo, A., et al. (2020). Processing of Sr^{2+} containing poly L-lactic acid-based hybrid composites for additive manufacturing of bone scaffolds. *Front. Mater.* 7:601645. doi: 10.3389/fmats.2020.601645

Mondal, S., Nguyen, T. P., Pham, V. H., Hoang, G., Manivasagan, P., Kim, M. H., et al. (2020). Hydroxyapatite nano bioceramics optimized 3D printed poly lactic acid scaffold for bone tissue engineering application. *Ceram. Int.* 46, 3443–3455. doi: 10.1016/j.ceramint.2019.10.057

Montalbano, G., Borciani, G., Cerqueni, G., Licini, C., Banche-Niclot, F., Janner, D., et al. (2020). Collagen hybrid formulations for the 3D printing of nanostructured bone scaffolds: an optimized genipin-crosslinking strategy. *Nanomaterials* 10:1681. doi: 10.3390/nano10091681

Nie, W., Peng, C., Zhou, X., Chen, L., Wang, W., Zhang, Y., et al. (2017). Three-dimensional porous scaffold by self-assembly of reduced graphene oxide and nano-hydroxyapatite composites for bone tissue engineering. *Carbon N. Y.* 116, 325–337. doi: 10.1016/j.carbon.2017.02.013

Oh, S. H., Park, I. K., Kim, J. M., and Lee, J. H. (2007). *In vitro* and *in vivo* characteristics of PCL scaffolds with pore size gradient fabricated by a centrifugation method. *Biomaterials* 28, 1664–1671. doi: 10.1016/j.biomaterials.2006.11.024

Peñarrocha-Diago, M., Bernabeu-Mira, J. C., Fernández-Ruíz, A., Aparicio, C., and Peñarrocha-Oltra, D. (2020). Bone regeneration and soft tissue enhancement around zygomatic implants: retrospective case series. *Materials* 13:1577. doi: 10.3390/ma13071577

Peng, L., Cheng, X. R., Wang, J. W., Xu, D. X., and Wang, G. (2016). Preparation and evaluation of porous chitosan/collagen scaffolds for periodontal tissue engineering. *J. Bioact. Compat. Poly.* 21, 207–220. doi: 10.1177/0883911506065100

Peter, M., Binulal, N. S., Nair, S. V., Selvamurugan, N., Tamura, H., and Jayakumar, R. (2010). Novel biodegradable chitosan–gelatin/nano-bioactive glass ceramic composite scaffolds for alveolar bone tissue engineering. *Chem. Eng. J.* 158, 353–361. doi: 10.1016/j.cej.2010.02.003

Raynald, Shu, B., Liu, X. B., Zhou, J. F., Huang, H., Wang, J. Y., Sun, X. D., et al. (2019). Polypyrrole/polylactic acid nanofibrous scaffold cotransplanted with bone marrow stromal cells promotes the functional recovery of spinal cord injury in rats. *CNS Neurosci. Ther.* 25, 951–964. doi: 10.1111/cns.13135

Ribeiro, T. O., Silveira, B. M., Meira, M. C., Carreira, A.C. O., Sogayar, M. C., Meyer, R., et al. (2019). Investigating the potential of the secretome of mesenchymal stem cells derived from sickle cell disease patients. *PLoS ONE* 14:e0222093. doi: 10.1371/journal.pone.0222093

Roosa, S. M., Kemppainen, J. M., Moffitt, E. N., Krebsbach, P. H., and Hollister, S. J. (2010). The pore size of polycaprolactone scaffolds has limited influence on bone regeneration in an *in vivo* model. *J. Biomed. Mater. Res. A* 92, 359–368. doi: 10.1002/jbm.a.32381

Saleem, M., Rasheed, S., and Yougen, C. (2020). Silk fibroin/hydroxyapatite scaffold: a highly compatible material for bone regeneration. *Sci. Technol. Adv. Mater.* 21, 242–266. doi: 10.1080/14686996.2020.1748520

Sharmila, G., Muthukumaran, C., Kirthika, S., Keerthana, S., Kumar, N. M., and Jeyanthi, J. (2020). Fabrication and characterization of *Spinacia oleracea* extract incorporated alginate/carboxymethyl cellulose microporous scaffold for bone tissue engineering. *Int. J. Biol. Macromol.* 156, 430–437. doi: 10.1016/j.ijbiomac.2020.04.059

Shen, J., Chen, B., Zhai, X., Qiao, W., Wu, S., Liu, X., et al. (2021). Stepwise 3D-spatio-temporal magnesium cationic niche: nanocomposite scaffold mediated microenvironment for modulating intramembranous ossification. *Bioact. Mater.* 6, 503–519. doi: 10.1016/j.bioactmat.2020.08.025

Shi, X., Sitharaman, B., Pham, Q. P., Liang, F., Wu, K., Edward Billups, W., et al. (2007). Fabrication of porous ultra-short single-walled carbon nanotube nanocomposite scaffolds for bone tissue engineering. *Biomaterials* 28, 4078–4090. doi: 10.1016/j.biomaterials.2007.05.033

Shie, M. Y., and Ding, S. J. (2013). Integrin binding and MAPK signal pathways in primary cell responses to surface chemistry of calcium silicate cements. *Biomaterials* 34, 6589–6606. doi: 10.1016/j.biomaterials.2013.05.075

Smith, C. A., Richardson, S. M., Eagle, M. J., Rooney, P., Board, T., and Hoyland, J. A. (2015). The use of a novel bone allograft wash process to generate a biocompatible, mechanically stable and osteoinductive biological scaffold for use in bone tissue engineering. *J. Tissue Eng. Regen. Med.* 9, 595–604. doi: 10.1002/term.1934

Sukhodub, L. B., Yanovska, G. O., Kuznetsov V. M., Martynyuk, O. O., and Sukhodub, L.F. (2016). Injectable biopolymer-hydroxyapatite hydrogels: obtaining and their characterization. *J. Nano Electr. Phys.* 8:01032. doi: 10.21272/jnep.8(1).01032

Tohamy, K. M., Mabrouk, M., Soliman, I. E., Beherei, H. H., and Aboelnasr, M. A. (2018). Novel alginate/hydroxyethyl cellulose/hydroxyapatite composite scaffold for bone regeneration: *in vitro* cell viability and proliferation of human mesenchymal stem cells. *Int. J. Biol. Macromol.* 112, 448–460. doi: 10.1016/j.ijbiomac.2018.01.181

Uccelli, A., Wolff, T., Valente, P., Di Maggio, N., Pellegrino, M., Gurke, L., et al. (2019). Vascular endothelial growth factor biology for regenerative angiogenesis. *Swiss Med. Wkly.* 149:w20011. doi: 10.4414/smw.2019.20011

Wei, J., Wang, Y., Jiang, J., Yan, Y., Fan, D., Yang, X., et al. (2019). Development of an antibacterial bone graft by immobilization of levofloxacin hydrochloride-loaded mesoporous silica microspheres on a porous scaffold surface. *J. Biomed. Nanotechnol.* 15, 1097–1105. doi: 10.1166/jbn.2019.2743

Wei, S., Ma, J. X., Xu, L., Gu, X. S., and Ma, X. L. (2020). Biodegradable materials for bone defect repair. *Mil. Med. Res.* 7:54. doi: 10.1186/s40779-020-00280-6

Wijesinghe, W. P. S. L., Mantilaka, M. M. M. G. P. G., Rajapakse, R. M. G., Pitawala, H. M. T. G. A., Premachandra, T. N., Herath, H. M. T. U., et al. (2017). Urea-assisted synthesis of hydroxyapatite nanorods from naturally occurring impure apatite rocks for biomedical applications. *RSC Adv.* 7, 24806–24812. doi: 10.1039/C7RA02166F

Windhager, R., Hobusch, G. M., and Matzner, M. (2017). Allogeneic transplants for biological reconstruction of bone defects. *Orthopade* 46, 656–664. doi: 10.1007/s00132-017-3452-0

Witek, L., Shi, Y., and Smay, J. (2017). Controlling calcium and phosphate ion release of 3D printed bioactive ceramic scaffolds: an *in vitro* study. *J. Adv. Ceram.* 6, 157–164. doi: 10.1007/s40145-017-0228-2

Yang, J., Wang, Q, Wang, Y., Han, S., Yao, J., Shao, S., et al. (2015). Preparation and *in vitro* release of multilayer alginate chitosan microspheres loading VEGF and vancomycin. *Chem. J. Chin. Univ.* 36, 1025–1032. doi: 10.7503/cjcu20140992

You, Y., Keqiqu, Huang, Z., Ma, R., Shi, C., Li, X., Liu, D., et al. (2019). Sodium alginate templated hydroxyapatite/calcium silicate composite adsorbents for efficient dye removal from polluted water. *Int. J. Biol. Macromol.* 141, 1035–1043. doi: 10.1016/j.ijbiomac.2019.09.082

Yu, L., Fei, Q., Lin, J., Yang, Y., and Xu, Y. (2020). The osteogenic effect of local delivery of vancomycin and tobramycin on bone marrow stromal cells. *Infect. Drug Resist.* 13, 2083–2091. doi: 10.2147/IDR.S261767

Zhang, C., Shao, K, Liu, C., Li, C., and Yu, B. (2019). Hypoxic Preconditioning BMSCs-exosomes inhibit cardiomyocyte apoptosis after acute myocardial infarction by upregulating microRNA-24. *Eur. Rev. Med. Pharmacol. Sci.* 23, 6691–6699. doi: 10.26355/eurrev_201908_18560

Zhou, X., Weng, W., Chen, B., Feng, W., Wang, W., Nie, W., et al. (2018). Mesoporous silica nanoparticles/gelatin porous composite scaffolds with localized and sustained release of vancomycin for treatment of

infected bone defects. *J. Mater. Chem. B* 6, 740–752. doi: 10.1039/C7TB01246B

Zima, A., Czechowska, J., Szponder, T., and Slosarczyk, A. (2020). *In vivo* behavior of biomicroconcretes based on alpha-tricalcium phosphate and hybrid hydroxyapatite/chitosan granules and sodium alginate. *J. Biomed. Mater. Res. A* 108, 1243–1255. doi: 10.1002/jbm.a.36898

Zou, Z., Wang, L., Zhou, Z., Sun, Q., Liu, D., Chen, Y., et al. (2021). Simultaneous incorporation of PTH(1-34) and nano-hydroxyapatite into Chitosan/Alginate Hydrogels for efficient bone regeneration. *Bioact. Mater.* 6, 1839–1851. doi: 10.1016/j.bioactmat.2020.11.021

Conflict of Interest: The authors declare that the research was conducted in the absence of any commercial or financial relationships that could be construed as a potential conflict of interest.